Report

www.the-innovation.org

Spin engineering of single-site metal catalysts

Zichuang Li,[1,2] Ruguang Ma,[1,3,*] Qiangjian Ju,[1,2] Qian Liu,[1,2] Lijia Liu,[4] Yufang Zhu,[1,2] Minghui Yang,[5] and Jiacheng Wang[1,2,6,*]

*Correspondence: maruguang@mail.sic.ac.cn (R.M.); jiacheng.wang@mail.sic.ac.cn (J.W.)

Received: November 9, 2021; Revised: June 6, 2022; Accepted: June 6, 2022; Published Online: June 9, 2022; https://doi.org/10.1016/j.xinn.2022.100268

GRAPHICAL ABSTRACT

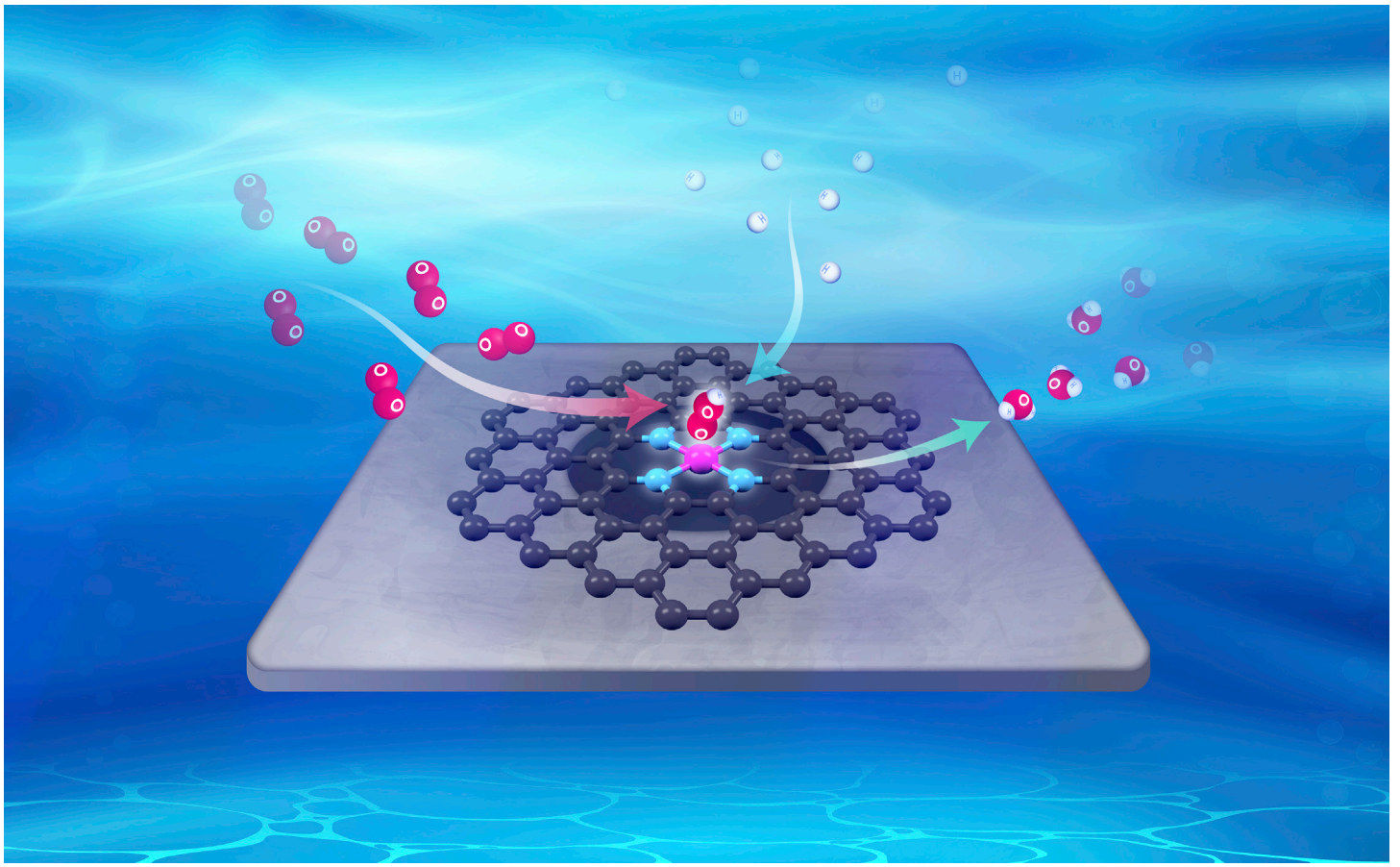

PUBLIC SUMMARY

- Single-site FeN_4 species are designed to dangle over axial carbon micropores (d-FeN_4)
- d-FeN_4 shows much superior oxygen reduction reactivity to traditional FeN_4
- d-FeN_4 facilitates the formation of singlet-state oxygen-containing species with optimized spin states by micropore
- This work provides in-depth understanding of spin tuning for advanced catalyst design

Spin engineering of single-site metal catalysts

Zichuang Li,[1,2] Ruguang Ma,[1,3,*] Qiangjian Ju,[1,2] Qian Liu,[1,2] Lijia Liu,[4] Yufang Zhu,[1,2] Minghui Yang,[5] and Jiacheng Wang[1,2,6,*]

[1]State Key Laboratory of High-Performance Ceramics and Superfine Microstructure, Shanghai Institute of Ceramics, Chinese Academy of Sciences, 1295 Dingxi Road, Shanghai 200050, China

[2]Center of Materials Science and Optoelectronics Engineering, University of Chinese Academy of Sciences, Beijing 100049, China

[3]School of Materials Science and Engineering, Suzhou University of Science and Technology, 99 Xuefu Road, Suzhou 215009, China

[4]Department of Chemistry, Western University, 1151 Richmond Street, London, ON N6A 5B7, Canada

[5]Ningbo Institute of Materials Technology and Engineering, Chinese Academy of Sciences, 1219 Zhongguan West Road, Ningbo 315201, China

[6]Hebei Provincial Key Laboratory of Inorganic Nonmetallic Materials, College of Materials Science and Engineering, North China University of Science and Technology, Tangshan 063210, China

*Correspondence: maruguang@mail.sic.ac.cn (R.M.); jiacheng.wang@mail.sic.ac.cn (J.W.)

Received: November 9, 2021; Revised: June 6, 2022; Accepted: June 6, 2022; Published Online: June 9, 2022; https://doi.org/10.1016/j.xinn.2022.100268

Citation: Li Z., Ma R., Ju Q., et al., (2022). Spin engineering of single-site metal catalysts. The Innovation **3(4)**, 100268.

Single-site metal atoms (SMAs) on supports are attracting extensive interest as new catalytic systems because of maximized atom utilization and superior performance. However, rational design of configuration-optimized SMAs with high activity from the perspectives of fundamental electron spin is highly challenging. Herein, N-coordinated Fe single atoms are successfully distributed over axial carbon micropores to form dangling-FeN_4 centers (d-FeN_4). This unique d-FeN_4 demonstrates much higher intrinsic activity toward oxygen reduction reaction (ORR) in $HClO_4$ than FeN_4 without micropore underneath and commercial Pt/C. Both theoretical calculation and electronic structure characterization imply that d-FeN_4 endows central Fe with medium spin ($t_{2g}^4 e_g^1$), which provides a spin channel for electron transition compared with FeN_4 with low spin. This leads to the facile formation of the singlet state of oxygen-containing species from triplet oxygen during the ORR, thus showing faster kinetics than FeN_4. This work provides an in-depth understanding of spin tuning on SMAs for advanced energy catalysis.

INTRODUCTION

The sluggish kinetics of the oxygen reduction reaction (ORR) is a notorious bottleneck for the scalable application of metal-air batteries and fuel cells, which may arise from multiple intermediate steps and high dissociation energy of O=O double bond.[1,2] Although platinum (Pt)-based catalysts exhibit excellent performance toward ORR, the limited reserve and high price of Pt have stimulated the exploration of non-precious electrocatalysts.[3–5] Among various non-precious ORR electrocatalysts, single-site Fe coordinated with nitrogen atoms (e.g., FeN_4) has attracted much attention because the unoccupied 3d orbitals in central Fe can reduce the bond strength between active site and oxygen-containing intermediates.[6]

However, traditional FeN_4 with symmetric configuration generally suffers from unfavorable O_2 adsorption and dissociation, leading to unsatisfactory activity, especially in acidic solution. Therefore, various strategies have been investigated by combining experimental with theoretical to improve the ORR performance of FeN_4 sites. One versatile strategy of doping selective atoms (e.g., sulfur) or implanting secondary metal-N_x can downshift the d-band center of Fe by withdrawing electrons.[7,8] Another strategy is regulating the geometric structures either in the Fe-N_x basal plane or in the perpendicular direction. With regard to basal plane configuration, a typical pore-forming route was designed to form edge-sited FeN_4 moieties, which breaks the symmetry of electron distribution to boost electron transfer.[9–11] As for the axial direction of Fe-N_x plane, Chen et al.[12] constructed an axial Fe-O coordination to evoke electronic localization among the axial direction of O-FeN_4 sites, thus improving O_2 adsorption and activation. Li et al.[13] prepared a N-FeN_4C_{10} moiety and revealed that the fifth coordinating N atom renders a larger 3d electron density of high-spin Fe^{2+} located out of the N_4 plane. Furthermore, a local contraction strain by off-plane ripples could trigger the positive shift of 3d orbitals of central Fe in FeN_4, facilitating O_2 adsorption.[14] The aforementioned studies broaden the family and promote the development of FeN_4 electrocatalysts. However, the exploration of new configuration and in-depth understanding of FeN_4 from the perspective of fundamental electron spin-orbit coupling are still desirable.

From the viewpoint of orbital physics, these strategies of changing the in-plane or off-plane configurations can be unified by engineering local spin states.[15,16] As for Fe-N_x configuration, central Fe cation possesses multiple spin configurations, including low spin state ($t_{2g}^5 e_g^0$), intermediate spin state ($t_{2g}^4 e_g^1$), and high spin state ($t_{2g}^3 e_g^2$), where the low spin and intermediate spin states can penetrate the antibonding π orbital of O_2, rendering high ORR activity.[13,17] As the ground spin state of O_2 is a spin triplet with two unpaired electrons (↑O=O↑), whereas the ground spin state of OH^-/H_2O reactants is a singlet without unpaired electrons, the reaction kinetics of ORR with a spin transition is theoretically slow.[17] To accelerate the electron transfer with spin transition, the additional energy or internal structure design is highly required.[18] For spin-aligned electrocatalysts, such a spin-selective transition process would promote a spin polarization in the oxygen-redox process to facilitate the conversion between triplet oxygen and singlet OH^-/H_2O.[19] Therefore, it is attractive to design new FeN_4 configuration with appropriate spin state to promote the spin-selective electron transfer and obtain the lower energy barrier (~1 eV) from oxygen with the triplet ground state to its next excited state.[20]

Herein, we successfully prepared a novel SMA electrocatalyst with dangling FeN_4 sites (d-FeN_4) and superior activity for acidic ORR, in which FeN_4 sites were uniformly dispersed over micropores. Compared with FeN_4 without micropores underneath, theoretical calculations reveal that the Fe in d-FeN_4 possesses stronger electron localization and more overlap of density of states (DOS) with O_2. Moreover, the measured magnetic susceptibility illustrates that the intermediate spin configuration of d-FeN_4, where the unpaired electron in d-FeN_4 and O_2 could couple and fill in σ orbital and π orbital, leading to facile formation of singlet state. Such a dangling Fe site in d-FeN_4 could boost spin hopping of electrons from triplet O_2 to singlet oxygen-containing intermediates (*OOH, *O, and *OH). Thus, the d-FeN_4 sites show much superior ORR activity in acidic $HClO_4$ than FeN_4 because of increasing O_2 dissociation ability and lowering energy barrier. This work opens a new avenue for the design of high-performance oxygen-redox electrocatalysts by engineering electron spin transition induced by carbon micropores underneath.

RESULTS AND DISCUSSION

Synthesis and microstructure of d-FeN_4

The adsorption-pyrolysis process of d-FeN_4 is illustrated in Figure 1A. Carbon materials with abundant micropores (Figure S1) were used as the carriers to capture FePc molecules on the basis of the adsorption effect. This micropore-rich substrate acts as a site-selective capture for FePc molecules, which is certified by the thermodynamic calculation in Figure 1B. The adsorption energy at the pore sites is about −0.98 eV, indicating a favorable adsorption with 0.94 eV at the plane sites. Under pyrolysis conditions, the adsorbed FePc molecules could convert to the d-FeN_4 configuration in which the resulting single-site Fe atoms are freely distributed over carbon micropores. The variation trend of micropore content definitely confirms the aforementioned formation process. Because a great number of micropores are blocked with FePc-derived FeN_4 species, the specific surface area (SSA) decreases remarkably. Figure 1C clearly displays the sharp change of SSA from 1,334 m^2/g MC to 523.5 m^2/g d-FeN_4. In contrast, the control sample MC-700 prepared by pyrolysis of MC at 700°C without FePc molecules possesses a comparable SSA of 1,338 m^2/g to MC (1,334 m^2/g) (Figure S2). This strongly suggests that the adsorption and conversion of FePc molecules on the micropore dominate the decrease of SSA. Meanwhile, an obvious drop can be seen at low pressure, suggesting the disappearance of a mass of micropores. It is also remarkable that pore volume less than 2 nm occurs

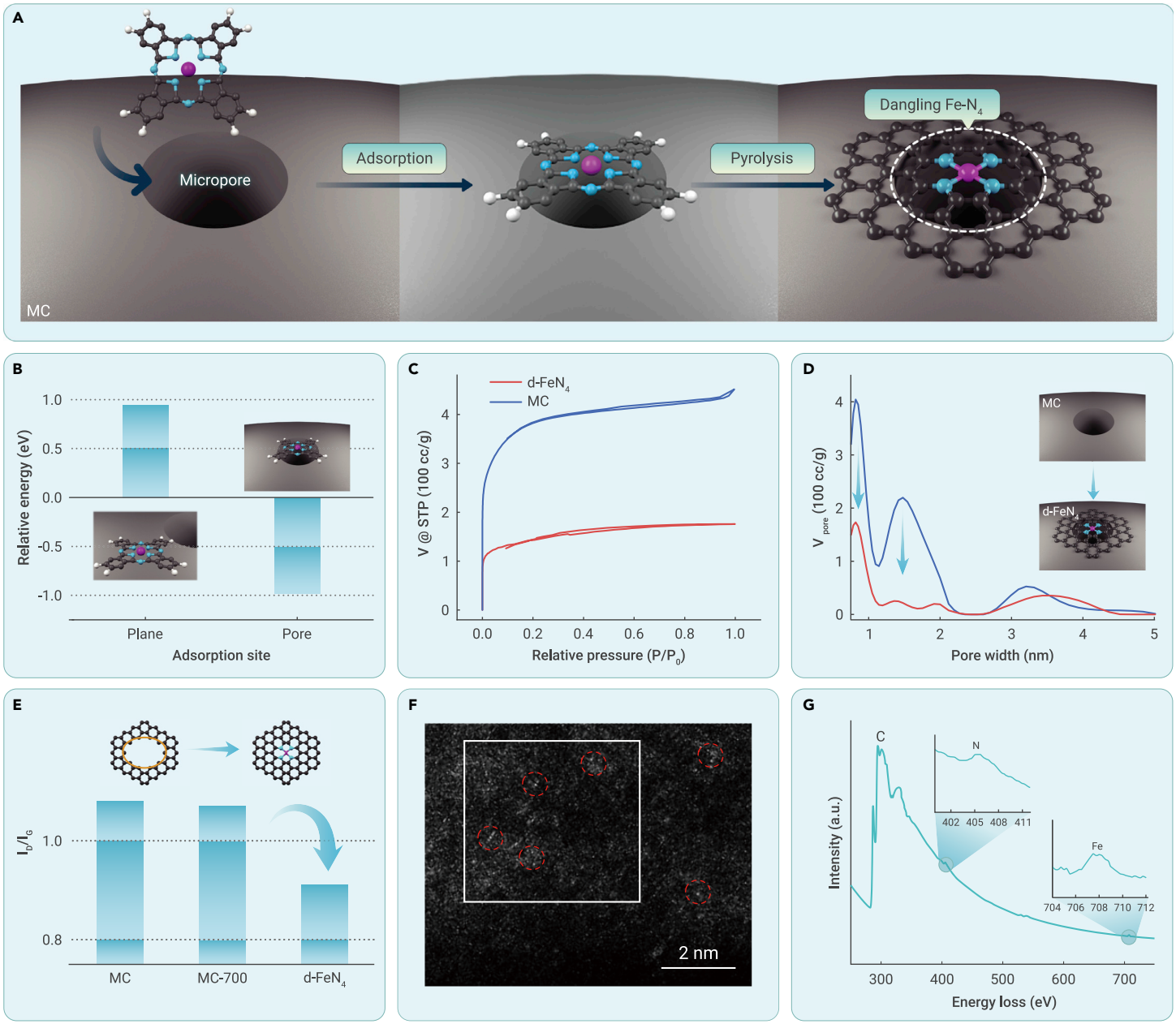

Figure 1. Synthesis and structural characterization of d-FeN_4 (A) Schematic diagram of the synthesis of d-FeN_4 through an adsorption-pyrolysis process. Purple, cyan, black, and white spheres represent Fe, N, C, and H atoms, respectively. (B) The relative energy of FePc adsorbed at the pore site and plane site in microporous carbons (MCs). (C and D) N_2 isothermal sorption isotherms (C) and (D) pore size distribution curves for MC and d-FeN_4. The results show that covering the micropores by FeN_4 species resulted in the significant decrease in the amount of nitrogen adsorption. (E) The contents of defective carbon of MC, MC-700, and d-FeN_4 according to Raman spectra. (F and G) HAADF-STEM image (F) and (G) EELS of d-FeN_4 from white dotted line marked area in (F).

obviously diving, as marked by the arrows in Figure 1D and Table S2, which is attributed to the patched FeN_4 species. In detail, the cumulative volume less than 2 nm of MC is 0.533 mL/g, much larger than 0.174 mL/g of d-FeN_4, showing a decreasing volume about 67.4% because of d-FeN_4 covering on the micropore. On the other hand, Raman spectra also confirm the change of microstructure (Figure S3). The intensity ratio of the D band (1,350 cm^{-1}) to G band (1,580 cm^{-1}) decreases from 1.08 for MC to 0.91 for d-FeN_4, as summarized in Figure 1E, which demonstrates that MC possesses more intrinsic defects than d-FeN_4. With regard to the control sample, the value for MC-700 is 1.07, similar to MC. This suggests that the lower ratio for d-FeN_4 originates from the adsorption and conversion of FePc above the pore.

To further analyze the single-atom d-FeN_4, high-angle annular dark field scanning transmission electron microscopy (HAADF-STEM) was used. The HAADF-STEM image reveals the atomic Fe in d-FeN_4 sample because of the separate bright dots marked with red cycles (Figure 1F). Electron energy loss spectroscopy (EELS) at the white dotted line-marked region in Figure 1F demonstrates the co-existence of N and Fe as two peaks at 400 and 708 eV (Figure 1G). In addition, no Fe peaks can be observed in the XRD spectrum (Figure S4). This is consistent with the observation by HAADF-STEM, indicating that there is no agglomeration of Fe. The signal at g = 3.03 in the EPR spectrum is the fingerprint of the atomic FeN_4 moieties (Figure S5).[21] All above results suggest that the atomically dispersed FeN_4 sites have been achieved. In addition, the same contents of C-N bonds in d-FeN_4 and FeN_4 illustrate that there are no edged FeN_4 sites (Figure S6; Table S3).[22] By tuning the FePc content, the loading amount of d-FeN_4 can also be regulated, of which the maximum is about 1.07 wt %, as confirmed by XPS (Figure S7).

Spin state of electrons in d-FeN_4

The local structure of d-FeN_4 was further unveiled by X-ray absorption near-edge structure (XANES) and extended X-ray absorption fine structure. The absorption edges of d-FeN_4 and FeN_4 K-edge XANES load between Fe foil and Fe_2O_3 (Figure 2A), indicating that the valence of Fe in d-FeN_4 and FeN_4 is situated between 0 and +3. Higher valence of Fe in d-FeN_4 originates from the shift to the higher energy direction, as shown by the enlarged spectra (Figure 2A, inset). As

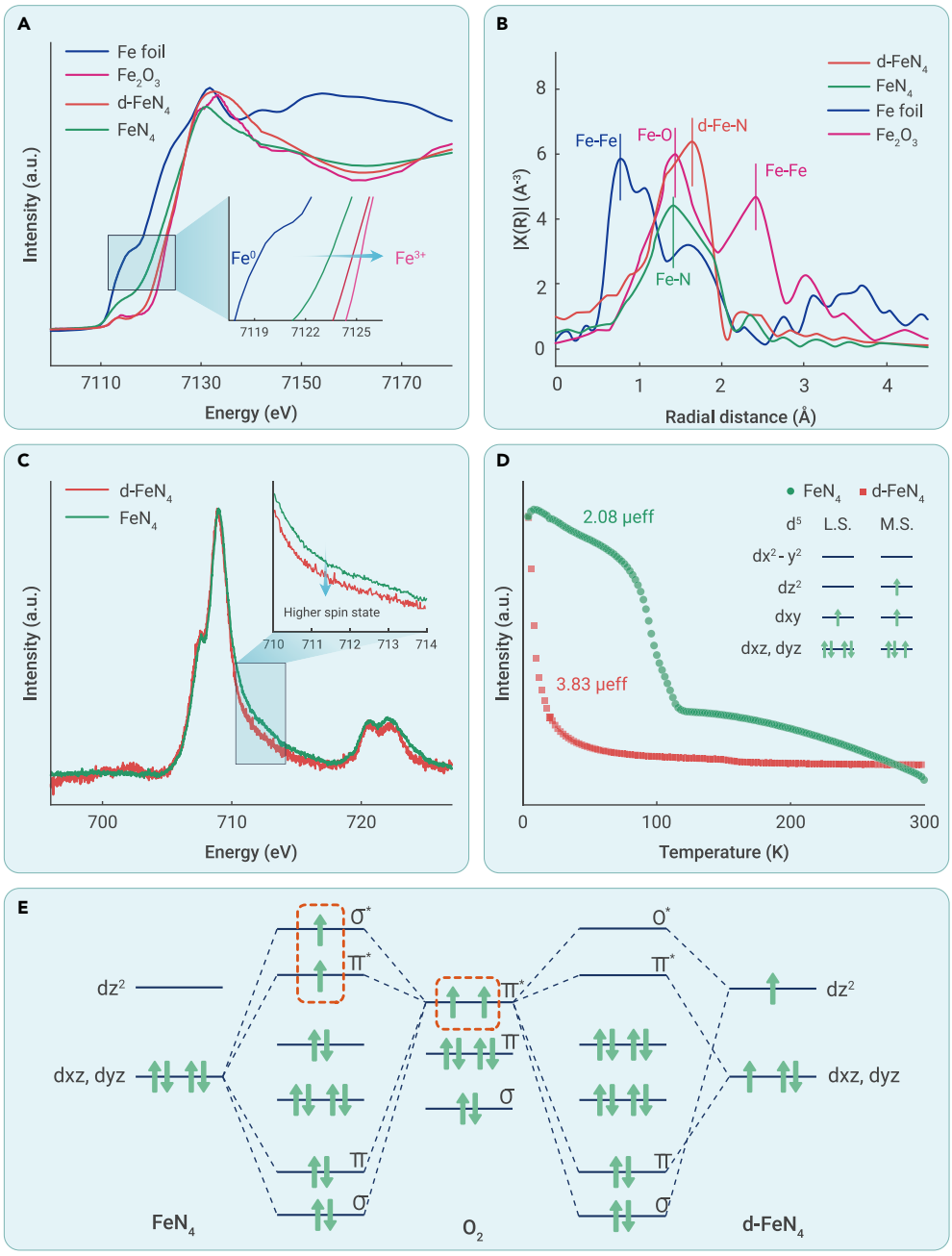

Figure 2. Electronic structure analyses of FeN_4 and d-FeN_4 (A) The Fe K-edge XANES curves of Fe foil, Fe_2O_3, d-FeN_4, and FeN_4. (B) The Fe K-edge EXAFS of Fe foil, Fe_2O_3, FeN_4, and d-FeN_4, plotted at the R-space. (C) The Fe L-edge XANES of d-FeN_4 and FeN_4. (D) Magnetic susceptibility of d-FeN_4 and FeN_4. The inset shows the illustration of electrons filling in d orbitals. (E) Molecular orbital diagram of oxygen adsorbed at d-FeN_4 and FeN_4.

high-resolution Fe 2p XPS spectra displayed in Figure S8, the peaks of Fe 2p spectrum can be ascribed to Fe^{3+} and Fe^{2+} through deconvolution. The relative content of Fe^{3+} increases from 55% of FeN_4 to 66% of d-FeN_4. The calculated valence state of Fe in d-FeN_4 is +2.7, which is higher than +2.1 of Fe in FeN_4 but smaller than +3 of Fe_2O_3 (Figure S9). The Fe EXAFS reveal that signal of Fe-N coordination shifts positively, indicating a lengthened Fe-N bond (Figure 2B). By calculating the first derivative, the "shoulder" of XANES between 7,110 and 7,140 eV originating from the band structure becomes more obvious.[23] As shown in Figure S10, the curve of d-FeN_4 shows a large value around 7,125–7,130 eV, indicating that d-FeN_4 has more high-energy electrons than FeN_4 without axis micropore. The same conclusion can be drawn by XAS of Fe L-edge. The higher intensity from 710 to 714 eV certifies higher spin of electrons in d-FeN_4 than FeN_4 (Figure 2C).[24]

The zero-field cooling temperature-dependent magnetic susceptibility was further measured to disclose the spin configuration of d-FeN_4 and FeN_4. As displayed in Figure 2D, the calculated effective magnetic moment of d-FeN_4 and FeN_4 is 3.83 μ_{eff} and 2.08 μ_{eff}, respectively. According to a previous report ($\mu_{eff} = \sqrt{n*(n+2)}$),[25] the number of unpaired d electron (n) of d-FeN_4 is about 3, showing three unpaired electrons filling in d_{z2}, d_{xy}, and d_{xz}, d_{yz} orbitals (Figure 2D, inset), leading to a medium spin state of d-FeN_4. Only one unpaired d electron for FeN_4 demonstrates that there is only a single unpaired electron filling in the d_{xy} orbital. Because of the symmetry conservation, the interactions between d_{x2-y2} and d_{xy} orbitals of Fe and the orbitals of oxygen are negligible.[26,27] As shown in Figure 2E, when oxygen with a triplet state is adsorbed at d-FeN_4 with a medium spin state, the unpaired electron in d-FeN_4 and oxygen could couple and fill in σ orbital and π orbital, leading to the formation of singlet state. However, for FeN_4, the unpaired electrons in oxygen molecule couple with electron in pairs of FeN_4, and the others can fill in σ* orbital and π* orbital.

Electrocatalytic ORR performance

The positive effect of medium-spin electrons in Fe during ORR was studied in 0.1 M $HClO_4$. Linear sweep voltammetry (LSV) was first performed by using a rotating disk electrode to evaluate the electrocatalytic activity as shown in Figure 3A. The as-synthesized d-FeN_4 shows a high half potential of 0.83 V, which is very close to 0.85 V of commercial Pt/C and far superior to traditional FeN_4. Besides, the equal onset potential (0.93 V) for both d-FeN_4 and Pt/C indicates a keen response at the d-FeN_4 sites during ORR process. The d-FeN_4 shows a similar Tafel slope of 73 mV dec^{-1} as Pt/C (64 mV dec^{-1}), which is far smaller than that of FeN_4 (135 mV dec^{-1}) (Figure 3B). It suggests that pore-induced spin flipping could markedly accelerate the dynamics process. After taking the loading of active sites into account, the TOF value indicates that the d-FeN_4 behaves the highest intrinsic activity (Figure 3C). The rotating ring-disk electrode test in Figure S12 demonstrates that d-FeN_4 behaves an equal excellent selectivity compared with Pt/C with an almost $4e^-$ process and low H_2O_2 yields (Figure 3D). More important, the current density of d-FeN_4 remains 91.1% after adding methanol, much higher than 76.3% of Pt/C, displaying a superior methanol tolerance (Figure 3E). On the other hand, d-FeN_4 shows the long-term stability with 89% of initial current over 10,000 s, much better than 72.6% of Pt/C (Figure 3F).

Electronic interaction between O_2 with FeN_4

Spin transfer of electrons is helpful for ORR, as all the intermediates (*OOH, *O, and *OH) are singlet state. To understand the electronic interaction of oxygen with FeN_4 and d-FeN_4, the electronic structures of were first analyzed using density functional theory calculations (Figure 4). The structure models of FeN_4 and d-FeN_4 are shown in Figures 4A and 4C, respectively. Upon the structure relaxation, Fe atom in the d-FeN_4 model dips obviously because of the presence of vertical micropore (Table S1). This d-FeN_4 over micropores leads to a longer Fe-N bond than traditional FeN_4, resulting in obvious electron loss from Fe (Figure S13). The more critical effects during the process of adsorbing oxygen were expounded by the electron localization functions and projected electronic densities of states (pDOS). As shown in Figures 4B and 4E, a stronger electron localization at the marked area with 0.17 can be observed around Fe atom in d-FeN_4. In

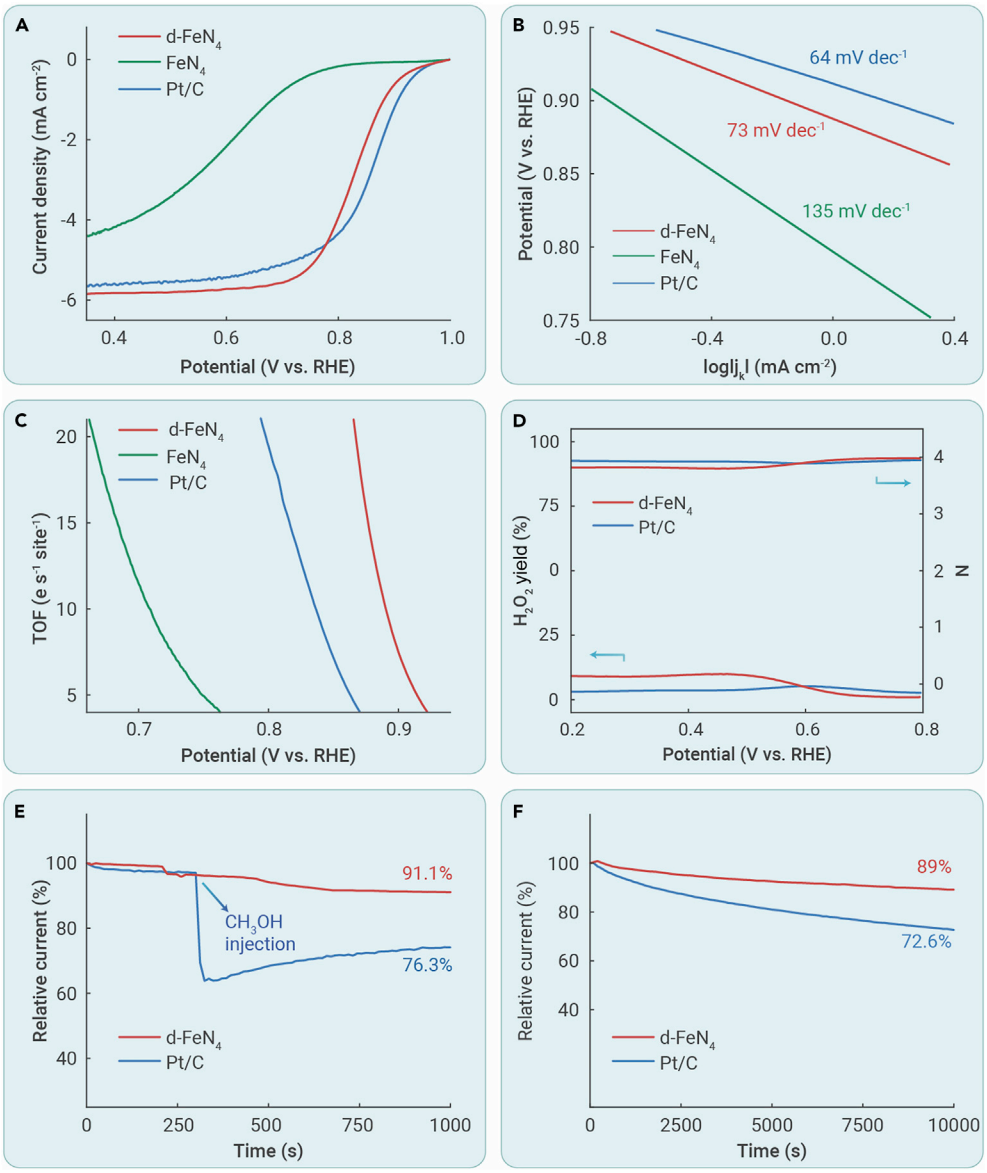

Figure 3. Electrocatalytic ORR measurements (A–C) LSV curves (A), (B) Tafel plots, and (C) TOF values of d-FeN_4, FeN_4, and Pt/C at 1,600 rpm in 0.1 M O_2-saturated $HClO_4$ electrolyte. (D–F) N (electron transfer number) and H_2O_2 yields (D), (E) methanol tolerance test, and (F) long-term stability of d-FeN_4 and Pt/C.

contrast, traditional FeN_4 displays only 0.08 at the same position, indicating that the micropore could modify the localization of electrons in d-FeN_4 and thus result in a stronger interaction between oxygen and active site.[12]

Then, the binding features between two sites and oxygen are demonstrated through pDOS as shown in Figures 4C and 4F. The energy levels of Fe β-spin d orbitals in d-FeN_4 and O β-spin 2p orbital match better than in FeN_4.[28] Such disparity can be clearly illustrated through integrating the matched region (Figure 4G). The integral value of d-FeN_4 is nearly 3-fold that of FeN_4 (0.34 versus 0.12). This shows that d-FeN_4 could adsorb oxygen in thermodynamics more easily than FeN_4 (Figure 4G). The CO-TPD curves in Figure S14 supports such conclusion experimentally. The peak located at 400 K can be attributed to the physical adsorption and the peak at a higher temperature is assigned to chemical adsorption. The chemical adsorption peak of d-FeN_4 emerges at 549 K, much higher than 515.5 K for FeN_4, illustrating strong binding between d-FeN_4 and O. In addition, the spin density of Fe in d-FeN_4 sites shows a higher spin state than that of Fe in FeN_4, suggesting that there is a spin channel around Fe in the d-FeN_4 site, while no channel with equal strength exists in FeN_4.[17]

Thermodynamically rate-determining step of ORR on d-FeN_4

DFT calculations were further used to gain deep insight into the improved ORR activity. The difference of O_2 configurations after adsorbed at FeN_4 and d-FeN_4 was studied. As shown in Figures 5A, 5B, and S15, the bond length of O_2 at d-FeN_4 is 1.48 Å, much longer than that at FeN_4 (1.28 Å), implying that the O=O bond at the d-FeN_4 site is activated more easily. Second, the distalis O atom at d-FeN_4 behaves a more negative Bader charge of −0.22 |e| than −0.12 |e| at FeN_4, which is beneficial for capturing H proton.[29] Both O=O bond length and Bader charge illustrate that O_2 adsorbed at d-FeN_4 could occur more easily hydrogenation and subsequent steps. The free-energy evolution further verifies the smooth ORR process (Figures 5C and 5D). Thanks to the elongated O=O bond and more negative charge, the change of Gibbs free energy (ΔG_{*OOH}) from O_2 to *OOH intermediate is only 0.15 eV at the d-FeN_4 site, much lower than 0.42 eV at FeN_4. In terms of the thermodynamic calculations, the rate-determining step at the d-FeN_4 site is from *OH to H_2O, requiring a driven energy of 0.26 eV, which is still lower than the RDS energy (0.42 eV) from O_2 to *OOH at FeN_4.

CONCLUSIONS

A specific dangling FeN_4 configuration (d-FeN_4), in which single-site Fe atoms were dispersed over carbon micropores, was successfully synthesized by adsorption of FePc on micropores and subsequent pyrolysis, which shows outstanding ORR activity in acidic solution. Both DFT calculation and electronic structure characterization show that this unique d-FeN_4 endows the central Fe atom with the medium spin state ($t_{2g}^4 e_g^1$) and provides a spin channel for the electron transition, leading to the facile formation of singlet state of oxygen-containing species (e.g., *OOH, *OH, and H_2O) from triplet O_2 during the ORR. The electrochemical experiments imply that the as-synthesized d-FeN_4 shows a comparable ORR activity and a much superior stability to commercial Pt/C in $HClO_4$ electrolyte, much better than traditional FeN_4 without underneath pore regulation. The theoretical calculation implied that the change of Gibbs free energy (ΔG_{*OOH}) from O_2 to *OOH intermediate is only 0.15 eV at the d-FeN_4 site, much lower than 0.42 eV at FeN_4. This further demonstrates high electrocatalytic activity and fast reaction kinetics for d-FeN_4 ascribed to optimized electron spin state induced by micropores underneath. The present strategy of catalyst design and synthesis could be also extended to other single-atom catalytic systems with great potentials in various energy conversion and storage devices.

MATERIALS AND METHODS

Chemicals

N-methylpyrrolidone (NMP) and iron phthalocyanine (FePc) were obtained from Aladdin. HCl and KOH were obtained from Sinopharm Chemical Reagent. Acetylene black was purchased from Guangdong Canrd New Energy Technology. Nafion solution (5 wt %) was purchased from Aldrich. Commercial 40 wt % Pt/C was obtained from Johnson Matthey. All chemicals were used as received without further purification.

Material synthesis

Synthesis of microporous carbon. Microporous carbon (MC) was synthesized according to previous literature.[30,31] First, bulky coals were broken and ground into powder in a mortar with a pestle. Two grams coal powder and 8 g KOH were placed in a mortar. After grinding for 0.5 h, the mixture was placed in a crucible and placed in a metal tube furnace. The powder was heated to 750°C for 2 h under Ar atmosphere. Finally, the product was kept

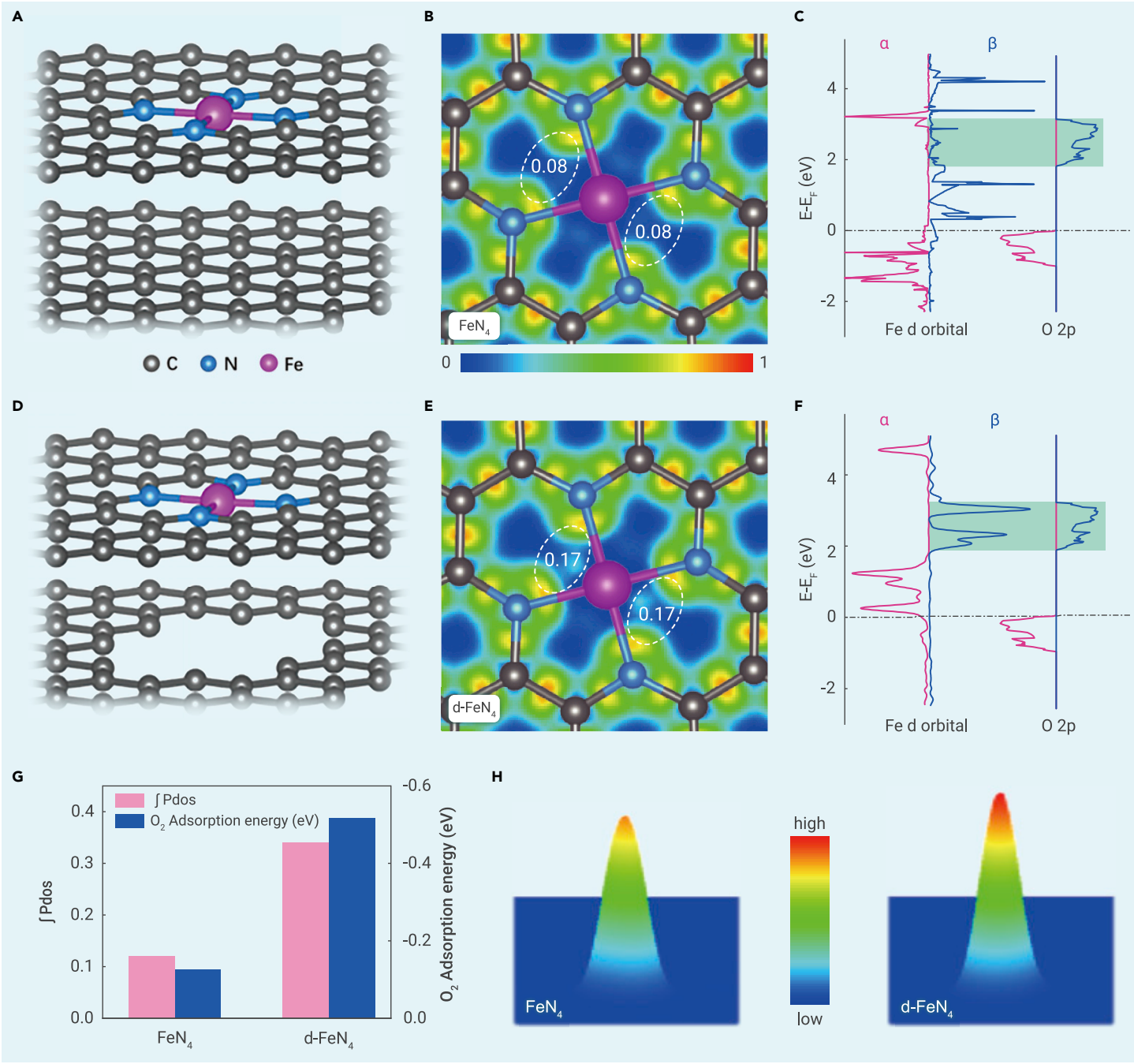

Figure 4. Theoretical calculation on electronic structures and oxygen-adsorption ability for FeN_4 and d-FeN_4 (A–F) Structure models, electron localization functions, and projected electronic densities of states (pDOS) of (A–C) FeN_4 and (D–F) d-FeN_4. (G) The integral of matched region in Fe β-spin d orbitals and oxygen adsorption energy at FeN_4 and d-FeN_4. (H) The spin densities of Fe in FeN_4 and d-FeN_4.

in 1 M HCl solution for 6 h to remove residual KOH and other impurities. Then, the product was washed by deionized water three times and named MC.

d-FeN₄ synthesis. MC (0.1 g) was dispersed in 20 mL NMP under ultrasonication for 2 h. Then, 10 mmol FePc was added into under stirring for 4 h and then left to stand for 12 h. The powder was filtered and then pyrolyzed at 700°C for 2 h under Ar atmosphere. Finally, the black solid was washed by 1 M HCl to remove the impurities. Changing the amount (x) of FePc could prepare other d-FeN_4-x samples (x = 0.03, 0.05, 0.07, or 0.12). For comparison, MC-700 was prepared by pyrolysis of MC at 700°C for 2 h under Ar atmosphere.

FeN₄ synthesis. The synthesis process of FeN_4 is similar to that of d-FeN_4. However, acetylene black instead of MC was used as the support.

Structure characterization

X-ray diffraction (XRD) was performed to determine the crystallographic structure with a Cu Kα (λ = 0.15405 nm) radiation source. Raman spectrometry was tested with a laser wavelength of 532 nm. X-ray photoelectron spectroscopy (XPS) was performed using an ESCALAB 250 X-ray photoelectron spectrometer with the Al Kα (hυ = 1486.6 eV) radiation source. The morphology and microstructure of the samples were observed using scanning electron microscopy (SEM; JEOL JSM-5610) and transmission electron microscopy (TEM; JEM-2100 F). Electron paramagnetic resonance (EPR) was performed using Bruker EMX spectrometer. Calculation of the spin number was based on a reference powder of Cu(II) TPP with 1 spin per molecule. The zero-field cooling (ZFC) temperature-dependent magnetic susceptibility was obtained using a vibrating sample magnetometer (VSM) with MPMS XL-7. The specific surface areas were obtained using the multipoint Brunauer-Emmett-Teller method. Pore size distribution curves, pore volume, and pore diameter were calculated by the desorption branch of the isotherms using the Barrett-Joyner-Halenda (BJH) method. X-ray absorption fine structure (XAFS) spectra at the Fe K-edge was obtained at the Advanced Photon Source (APS), beamline BM9. The samples were measured in X-ray fluorescence mode. The data were processed using the ATHENA program for background subtraction, normalization, and energy calibration.[32] The extended XAFS (EXAFS) was analyzed using the IFEFFIT package,[33] and EXAFS fitting was performed with FEFF6L.[34] A k range of

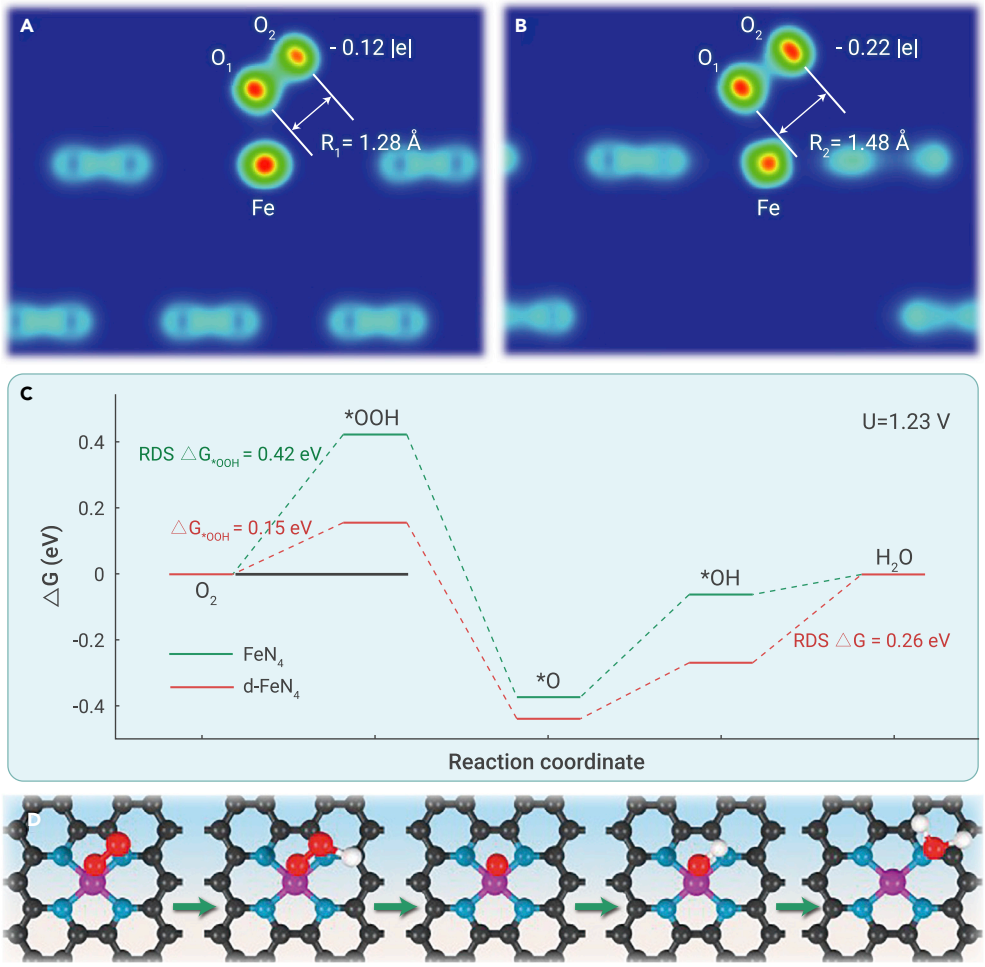

Figure 5. Thermodynamic insight into ORR activity increasement for d-FeN$_4$ (A and B) O=O bond length and Bader charge of distalis O after O_2 adsorbed at (A) FeN_4 and (B) d-FeN_4. (C) Free-energy evolution during ORR at d-FeN_4 and FeN_4. (D) Schematic illustration of ORR process. Purple, cyan, black, red, and white spheres represent Fe, N, C, O, and H atoms, respectively.

3.0–12.5 Å^{-1} was selected for the conversion to Fourier transform (FT)-EXAFS, which was the range subsequently used for EXAFS fitting. The Fe $L_{3,2}$-edge XANES was obtained at beamline 20A1 at the Taiwan Light Source, operated by the National Synchrotron Radiation Research Center (NSRRC). The spectra were obtained using the mode of total electron yield. The data were normalized to the incident photon flux.

Electrochemical measurements

Electrochemical measurements including cyclic voltammetry (CV), rotating disk electrode (RDE), rotating ring-disk electrode (RRDE), and chronoamperometric (CA) measurements were carried on an electrochemical workstation (AFMSRCE; Pine Research Instrumentation). All measurements were performed in the electrolyte of 0.1 M $HClO_4$ solution using a three-electrode system. A graphite rod and saturated calomel electrode (SCE) were used as the counter electrode and reference electrode, respectively. A rotating disk electrode (0.19625 cm^2 geometric surface area of glassy carbon) or rotating ring-disk electrode (0.2475 cm^2 geometric surface area of glassy carbon and 0.1866 cm^2 of Pt ring) coated with catalyst was used as the working electrode. Experimentally, the catalyst ink was prepared by adding 5 mg sample into 500 μL deionized water, 500 μL ethanol, and 20 μL Nafion (5 wt %) solution and then the solution was sonicated for 1 h. Then, 10 μL ink was dropped on the surface of the electrode and dried at 50°C, and another 10 μL ink was added and dried to form a thin film. Commercial 40 wt % Pt/C was prepared in the same way for comparison. The potentials versus SCE were converted to a reversible hydrogen electrode (RHE) scale. The conversion was calculated on the basis of the following equation:

$$E_{RHE} = E_{SCE} + 0.0591 \times pH + 0.242. \quad \text{(Equation 1)}$$

Before collecting the data, the electrode was activated using the CV measurement for 100 cycles with a scan rate of 100 mV s^{-1}. RRDE measurements were taken to evaluate the electron transfer number (n) and peroxide yields during ORR catalytic process. The equations are as follows:

$$n = \frac{4 * Id}{Id + Ir/N} \quad \text{(Equation 2)}$$

and

$$H_2O_2(\%) = \frac{200 * Ir}{N(Id + Ir/N)}, \quad \text{(Equation 3)}$$

where I_r is the ring current, I_d is the disk current, and N is the current collection efficiency of the Pt ring electrode.

The kinetic current density (J_K) was calculated using the equation

$$JK = \frac{JL * J}{JL - J}, \quad \text{(Equation 4)}$$

where J_L is the limiting diffusion current density, and J is the current density at a specific potential in the mixed-kinetic region.

DFT calculations

All density functional theory (DFT) calculations were performed using the Vienna Ab Initio Simulation Package (VASP).[35,36] The generalized gradient approximation method with the Perdew-Burke-Ernzerhof (PBE) exchange-correlation function was used to manage the electron exchange and correlation energy.[37] The plane wave basis (kinetic energy cut-off value 450 eV) was used to describe the valence electrons. A mesh of 1 × 1 × 1 was used for the k-point sampling obtained from the gamma center. The model is 22.14 × 22.14 × 36.8 Å^3, and the thickness of the vacuum layer is 20 Å. The atomic positions were fully optimized until the energy and forces converged to 1 × 10^{-5} eV and −0.0257 eV Å^{-1}, respectively. The calculations of pathways during ORR were conducted following the method used by Kulkarni et al.:[38]

$$O_2 * + H^+ + e^- \rightarrow * OOH, \quad \text{(Equation 5)}$$

$$* OOH + H^+ + e^- \rightarrow * O + H_2O, \quad \text{(Equation 6)}$$

$$O * + H^+ + e^- \rightarrow * OH, \quad \text{(Equation 7)}$$

and

$$*OH + H^+ + e^- \rightarrow H_2O + *, \quad \text{(Equation 8)}$$

where * stands for an active site on the catalytic surface.

The free energy ΔG of each step is obtained using the following equation:

$$\Delta G = \Delta E + \Delta E_{ZPE} - T\Delta S + \Delta G_U + \Delta G_{pH}, \quad \text{(Equation 9)}$$

where ΔE, ΔE_{ZPE}, and ΔS represent the different intermediate energy, zero-point energy changes, and entropy of the reaction, respectively. ΔE was obtained from DFT calculations, and ΔE_{ZPE} is the zero-point energy of each adsorbate or free molecules calculated by the vibrational frequency, T is the temperature, and ΔS is the entropy change. And the energy of H^+ is considered as 1/2 E_{H2}.

The bias effect on the free energy of each initial, intermediate, and final state involving electrons transfer in the electrode is also taken into account by shifting the energy of the state by:

$$\Delta G_U = -neU, \quad \text{(Equation 10)}$$

where U is the electrode applied potential, e is the transferred charge, and n is the number of proton-electron transferred pairs.

The change of free energy attributable to the effect of pH value of the electrolyte is considered by the correction of H^+ ions concentration dependence of the entropy

$$\Delta G_{pH} = -k_B T \ln[H^+] = pH * k_B T \ln 10, \quad \text{(Equation 11)}$$

where k_B is the Boltzmann constant.

REFERENCES

1. Li, Y., and Dai, H. (2014). Recent advances in zinc-air batteries. Chem. Soc. Rev. ***43***, 5257–5275.
2. Ma, R., Wang, J., Tang, Y., and Wang, J. (2022). Design strategies for single-atom iron electrocatalysts toward efficient oxygen reduction. J. Phys. Chem. Lett. ***13***, 168–174.
3. Guo, B., Ma, R., Li, Z., et al. (2020). Hierarchical N-doped porous carbons for Zn-air batteries and supercapacitors. Nanomicro Lett. ***12***, 20.
4. Yuan, Y., Adimi, S., Thomas, T., et al. (2021). Co_3Mo_3N - an efficient multifunctional electrocatalyst. Innovation ***2***, 100096.
5. Ma, R., Lin, G., Zhou, Y., et al. (2019). A review of oxygen reduction mechanisms for metal-free carbon-based electrocatalysts. NPJ Comput. Mater. ***5***, 78.
6. Shen, H., Peng, H., Yang, L., et al. (2021). Oxygen coordination on Fe-N-C to boost oxygen reduction catalysis. J. Phys. Chem. Lett. ***12***, 517–524.
7. Yang, G., Zhu, J., Yuan, P., et al. (2021). Regulating Fe-spin state by atomically dispersed Mn-N in Fe-N-C catalysts with high oxygen reduction activity. Nat. Commun. ***12***, 1734.
8. Mun, Y., Lee, S., Kim, K., et al. (2019). Versatile strategy for tuning ORR activity of a single Fe-N_4 Site by controlling electron-withdrawing/donating properties of a carbon plane. J. Am. Chem. Soc. ***141***, 6254–6262.
9. Ma, R., Lin, G., Ju, Q., et al. (2020). Edge-sited Fe-N_4 atomic species improve oxygen reduction activity via boosting O_2 dissociation. Appl. Catal. B Environ. ***265***, 118593.
10. Li, S., Ma, R., Pei, Y., et al. (2020). Geometric structure and electronic polarization synergistically boost hydrogen-evolution kinetics in alkaline medium. J. Phys. Chem. Lett. ***11***, 3436–3442.
11. Ramaswamy, N., Tylus, U., Jia, Q., and Mukerjee, S. (2013). Activity descriptor identification for oxygen reduction on nonprecious electrocatalysts: linking surface science to coordination chemistry. J. Am. Chem. Soc. ***135***, 15443–15449.
12. Chen, K., Liu, K., An, P., et al. (2020). Iron phthalocyanine with coordination induced electronic localization to boost oxygen reduction reaction. Nat. Commun. ***11***, 4173.
13. Li, X., Cao, C.-S., Hung, S.-F., et al. (2020). Identification of the electronic and structural dynamics of catalytic centers in single-Fe-atom material. Chem ***6***, 3440–3454.
14. Li, J., Zhang, H., Samarakoon, W., et al. (2019). Thermally driven structure and performance evolution of atomically dispersed FeN_4 sites for oxygen reduction. Angew. Chem. Int. Ed. ***58***, 18971–18980.
15. Nazmutdinov, R.R., Santos, E., and Schmickler, W. (2013). Spin effects in oxygen electrocatalysis: a discussion. Electrochem. Commun. ***33***, 14–17.
16. Orellana, W. (2013). Catalytic properties of transition metal-N_4 moieties in graphene for the oxygen reduction reaction: evidence of spin-dependent Mechanisms. J. Phys. Chem. C ***117***, 9812–9818.
17. Sun, Y., Sun, S., Yang, H., et al. (2020). Spin-related electron transfer and orbital interactions in oxygen electrocatalysis. Adv. Mater. ***32***, 2003297.
18. Wu, T., Ren, X., Sun, Y., et al. (2021). Spin pinning effect to reconstructed oxyhydroxide layer on ferromagnetic oxides for enhanced water oxidation. Nat. Commun. ***12***, 3634.
19. Ren, X., Wu, T., Sun, Y., et al. (2021). Spin-polarized oxygen evolution reaction under magnetic field. Nat. Commun. ***12***, 2608.
20. Torun, E., Fang, C.M., de Wijs, G.A., and de Groot, R.A. (2013). Role of magnetism in catalysis: RuO_2 (110) Surface. J. Phys. Chem. C ***117***, 6353–6357.
21. Liu, J.C., Ma, X., Li, Y., et al. (2018). Heterogeneous Fe_3 single-cluster catalyst for ammonia synthesis via an associative mechanism. Nat. Commun. ***9***, 1610.
22. Li, J., Jiao, L., Wegener, E., et al. (2020). Evolution pathway from iron compounds to Fe_1(II)-N_4 sites through gas-phase iron during pyrolysis. J. Am. Chem. Soc. ***142***, 1417–1423.
23. Wang, X., Jia, Y., Mao, X., et al. (2020). Edge-rich Fe-N_4 active sites in defective carbon for oxygen reduction catalysis. Adv. Mater. ***32***, 2000966.
24. Jiang, J., Ding, W., Li, W., et al. (2020). Freestanding single-atom-layer Pd-based catalysts: oriented splitting of energy bands for unique stability and activity. Chem ***6***, 431–447.
25. Kowalska, J.K., Nayyar, B., Rees, J.A., et al. (2017). Iron $L_{2,3}$-edge X-ray absorption and X-ray magnetic circular dichroism studies of molecular iron complexes with relevance to the FeMoCo and FeVCo active sites of nitrogenase. Inorg. Chem. ***56***, 8147–8158.
26. Wang, X., Ouyang, T., Wang, L., et al. (2019). Redox-inert Fe^{3+} ions in octahedral sites of Co-Fe spinel oxides with enhanced oxygen catalytic activity for rechargeable Zinc-Air batteries. Angew. Chem. Int. Ed. ***58***, 13291–13296.
27. Bockris, J., and Otagawa, T. (1984). The electrocatalysis of oxygen evolution on perovskites. J. Electrochem. Soc. ***131***, 290–302.
28. Li, X.-X., Cho, K.-B., and Nam, W. (2019). A theoretical investigation into the first-row transition metal-O_2 adducts. Inorg. Chem. Front. ***6***, 2071–2081.
29. Li, Z., Pei, Y., Ma, R., et al. (2021). A phosphate semiconductor-induced built-in electric field boosts electron enrichment for electrocatalytic hydrogen evolution in alkaline conditions. J. Mater. Chem. ***9***, 13109–13114.
30. Wang, J., and Kaskel, S. (2012). KOH activation of carbon-based materials for energy storage. J. Mater. Chem. ***22***, 23710.
31. Guo, S., Guo, B., Ma, R., et al. (2020). KOH activation of coal-derived microporous carbons for oxygen reduction and supercapacitors. RSC Adv. ***10***, 15707–15714.
32. Ravel, B., and Newville, M. (2005). *ATHENA*, *ARTEMIS*, *HEPHAESTUS*: data analysis for X-ray absorption spectroscopy using*IFEFFIT*. J. Synchrotron Radiat. ***12***, 537–541.
33. Newville, M. (2001). IFEFFIT: interactive XAFS analysis and FEFF fitting. J. Synchrotron Radiat. ***8***, 322–324.
34. Rehr, J.J., Mustre de Leon, J., Zabinsky, S.I., and Albers, R.C. (1991). Theoretical X-ray absorption fine structure standards. J. Am. Chem. Soc. ***113***, 5135–5140.
35. Kresse, G., and Hafner, J. (1993). Ab initio molecular dynamics for liquid metals. Phys. Rev. B Condens. Matter ***47***, 558–561.
36. Kresse, G., and Furthmüller, J. (1996). Efficiency of ab-initio total energy calculations for metals and semiconductors using a plane-wave basis set. Comput. Mater. Sci. ***6***, 15–50.
37. Kresse, G., and Joubert, D. (1999). From ultrasoft pseudopotentials to the projector augmented-wave method. Phys. Rev. B ***59***, 1758–1775.
38. Kulkarni, A., Siahrostami, S., Patel, A., and Nørskov, J.K. (2018). Understanding catalytic activity trends in the oxygen reduction reaction. Chem. Rev. ***118***, 2302–2312.

ACKNOWLEDGMENTS

We are grateful for financial support from the National Natural Science Foundation of China (grants 92163117, 52072389, and 52172058) and State Key Laboratory of ASIC & System (grant 2020KF002). J.W. thanks the Program of Shanghai Academic Research Leader (grant 20XD1424300) for financial support. L.L. acknowledges support from the Discovery Program of the Natural Sciences and Engineering Research Council of Canada (NSERC; grant DG RGPIN-2020-06675). Use of the Advanced Photon Source was supported by the U.S. Department of Energy, Office of Science, Office of Basic Energy Sciences, under contract DE-AC02-06CH11357. Technical support from APS beamline scientists Dr. George E. Sterbinsky and Dr. Tianpin Wu, and from TLS beamline scientist Dr. Lo-Yueh Chang, is greatly appreciated.

AUTHOR CONTRIBUTIONS

R.M. and J.W. conceived the idea. Z.L. and R.M. synthesized the samples and carried out the electrochemical experiments and DFT calculations. L.L. performed the XAFS measurements. Q.J., Q.L., Y.Z., and M.Y. analyzed the data and contributed to the scientific interpretation. Z.L., R.M., and J.W. wrote the manuscript. All authors commented on the manuscript.

DECLARATION OF INTERESTS

The authors declare no competing interests.

SUPPLEMENTAL INFORMATION

Supplemental information can be found online at https://doi.org/10.1016/j.xinn.2022.100268.

LEAD CONTACT WEBSITE

http://www.skl.sic.cas.cn/ktz/wjc/index.html.